J. Fluid Mech. (2013), *vol.* 722, *pp.* 187–213.
doi:10.1017/jfm.2013.89

Response of a hypersonic turbulent boundary layer to favourable pressure gradients

N. R. Tichenor[1],†, R. A. Humble[2] and R. D. W. Bowersox[2]

[1]Physics, Materials and Applied Mathematics Research, L.L.C., Tucson, AZ 85719, USA

[2]Department of Aerospace Engineering, Texas A&M University, College Station, TX 77843-3141, USA

(Received 29 January 2012; revised 7 October 2012; accepted 9 February 2013;
first published online 28 March 2013)

The role of streamline curvature-driven favourable pressure gradients in modifying the turbulence structure of a Mach 4.9, high-Reynolds-number ($Re_\theta = 43\,000$) boundary layer is examined. Three pressure gradient cases ($\beta = (\mathrm{d}p/\mathrm{d}x)(\delta^*/\tau_w) = 0.07, -0.3$ and -1.0) are characterized via particle image velocimetry. The expected stabilizing trends in the Reynolds stresses are observed, with a sign reversal in the Reynolds shear stress in the outer part of the boundary layer for the strongest favourable pressure gradient considered. The increased transverse normal strain rate and reduced principal strain rate are the primary factors. Reynolds stress quadrant events are redistributed, such that the relative differences between the quadrant magnitudes decreases. Very little preferential quadrant mode selection is observed for the strongest pressure gradient considered. Two-point correlations suggest that the turbulent structures are reoriented to lean farther away from the wall, accompanied by a slight reduction in their characteristic size, consistent with previous flow visualization studies. This reorientation is more pronounced in the outer, dilatation-dominated region of the boundary layer, whereas the alteration in structure size is more pronounced nearer the wall, where the principal strain rates are larger. In addition, integration of a simplified form of a Reynolds stress transport closure model provided a framework to assess the role of the strain-rate field on the observed Reynolds shear stresses. Given the simple geometry, the present data provide a suitable test bed for Reynolds stress transport and large-eddy model development and validation.

Key words: hypersonic, turbulent boundary layer, favourable pressure gradient

1. Introduction

Over the past few decades, considerable theoretical and experimental studies have been carried out to characterize boundary layers experiencing global mechanical distortions. The effects of convex curvature have attracted significant interest in particular, due to their often unexpected and spectacular stabilizing influence on flow properties across the boundary layer (see e.g. Bradshaw 1969, 1973). It is now fairly well known that such curvature inhibits turbulence, with the turbulence levels and wall friction decreasing relative to their canonical flat-plate values. Whereas for laminar flows, these effects have been shown to be first order, for turbulent flows

† Email address for correspondence: nathantichenor@gmail.com

the effects of wall curvature have been shown to be significantly larger; an order of magnitude larger than expected (see Bradshaw 1973). Spina, Smits & Robinson (1994) even postulated that relaminarization of part of the boundary layer is possible if the favourable pressure gradient is strong enough.

Although it has been known for some time that streamline curvature greatly affects the turbulence organization, few studies have carried out detailed whole-field measurements of this reorganization, and even fewer in the compressible flow regime. Under compressible flow conditions, there are additional complicating factors that must be considered. In addition to a favourable streamwise pressure gradient ($\partial p/\partial x < 0$), a surface-normal pressure gradient ($\partial p/\partial y > 0$), and streamwise curvature effects, where p is the static pressure and x and y are the wall-parallel and wall-normal directions, respectively; there is also bulk dilatation ($U_{k,k} > 0$), which has been shown to be a dominant strain rate in supersonic turbulent boundary layers (see e.g. Spina *et al.* 1994). Unsurprisingly, many authors have developed parameters to characterize these effects. The ratio of the extra strain rates (i.e. $\partial U/\partial x$, $\partial V/\partial y$, $\partial V/\partial x$, where U and V are the corresponding streamwise and transverse velocity components, respectively) to the principal strain rate $\partial U/\partial y$, called the distortion parameter d_{max}, was defined by Bradshaw (1974) as a means to classify a pressure gradient. A distortion is generally considered mild if $d_{max} < 0.01$ and strong for $d_{max} > 0.1$. If the distortion is applied for a time that is comparable to an eddy lifetime, Smits *et al.* (1989) suggested that an impulse parameter, which is a time-integrated strain rate, may be a better choice. Spina *et al.* (1994) defined two impulse parameters to characterize the distortion strength. For bulk dilatation, $I_p = \gamma^{-1} \ln(p_2/p_1)$ was defined, where the subscripts 1 and 2 correspond to the pressure before and after the imposed pressure gradient, respectively, and γ is the ratio of specific heats (=1.4 for air). For streamline curvature, $I_\phi = \Delta\phi$ was defined as the change in the wall angle, where ϕ is the local wall angle (in radians). Although these parameters have found utility in the characterization of high-speed turbulent boundary layers, it is generally acknowledged that their simple addition is unlikely to hold in any quantitative sense (Smits & Dussauge 2006).

A number of authors have experimentally investigated the influence of convex curvature-driven pressure gradients on high-speed turbulent boundary layers. Arnette, Samimy & Elliott (1995, 1998), experimentally tested four favourable pressure gradient cases at Mach 3 (centred and gradual expansions of 7 and 14°) using a combination of flow visualization and laser Doppler velocimetry (LDV). Similarly, Luker, Bowersox & Buter (2000) carried out detailed experiments on the mean and turbulent flow properties of a favourable pressure gradient boundary layer at Mach 2.9 using LDV. In related work, Ekoto *et al.* (2009) characterized two favourable pressure gradients at Mach 2.9, also incorporating the effects of surface roughness, by means of particle image velocimetry (PIV). Collectively, these studies showed that the axial turbulence intensities can decrease up to 70–90 % depending on the strength of the favourable pressure gradient.

One interesting observation to arise from this work was the sensitivity of the Reynolds shear stress to favourable pressure gradient. For example, Luker *et al.* (2000) observed an approximately 25 % reduction of Reynolds shear stress in the near-wall region, compared with the equivalent zero-pressure-gradient (ZPG) value. Yet the Reynolds shear stress response throughout the boundary layer was not the same. In the outer region (say $y/\delta > 0.5$, where δ is the boundary layer thickness), the kinematic Reynolds shear stress was typically negative, whereas the principal strain rates remained positive. A similar trend had been observed by Arnette *et al.* (1998).

The strain rate and associated extra production measurements of Luker *et al.* (2000) indicated that the overall turbulence production was negative in the outer half of the boundary layer, implying that energy was being fed from the fluctuating flow field back into the mean flow.

Conclusions have also been drawn regarding the effects of convex curvature on the coherent motions within the compressible turbulent boundary layer. The data obtained by Luker *et al.* (2000) indicated that the favourable pressure gradient resulted in lower turbulence levels with increased intermittency, which was interpreted to indicate that the large-scale structures were disintegrating into smaller ones. Using Rayleigh condensate scattering under the same flow conditions as the present study, Humble, Peltier & Bowersox (2012) also observed an increase in intermittency with favourable pressure gradient, with a movement of the onset of intermittency towards the edge of the boundary layer. Together with an overall decrease in intermittent flow region, they interpreted this to be associated with the less frequent penetration of irrotational fluid deep into the boundary layer, consistent with the idea that the boundary layer loses its ability to entrain free stream fluid as it negotiates the expansion.

Others have invoked arguments based on the conservation of angular momentum to explain the response of the flow structures, suggesting that when fluid elements pass through a supersonic expansion, their volume increases, resulting in reduced turbulence properties (see e.g. Dussauge & Gaviglio 1987; Arnette *et al.* 1998). Although the precise response(s) of the coherent motions to convex curvature remains an open question, the shear stress is mainly associated with the large-scale structures, and since the shear stress has been shown to reduce and/or change sign, it is reasonable to surmise that the structures are less coherent and that there is a redistribution of energy, despite their survival. However, since most of the available supersonic data that include both mean flow and turbulence measurements have been acquired between Mach 2–3, the effects of compressibility on the above trends remain unclear.

The aim of the present study is to experimentally examine the role of streamline curvature driven favourable pressure gradients in modifying the turbulence structure in a Mach 4.9, high-Reynolds-number ($Re_\theta = 43\,000$) boundary layer. Two favourable pressure gradients are compared with a canonical ZPG boundary layer, as well as with several lower-Mach-number studies in the literature. The steps in the study are to: (i) characterize the influence of the pressure gradients on the mean velocity and strain-rate field; (ii) quantify the role of the strain-rate field on the Reynolds stress turbulence statistics; and (iii) analyse the effect of the strain rates on the underlying turbulence structure via statistical analyses.

2. Experimental facility and flow conditions

2.1. *Flow facility*

The experiments were performed in the high-speed blow-down wind tunnel located at the National Aerothermochemistry Laboratory (NAL) at Texas A&M University. The two-dimensional wind tunnel nozzle was fabricated from stainless steel with exit dimensions of 7.62 cm × 7.62 cm. A schematic of the facility is shown in figure 1(*a*). The upstream (location 1) and downstream (location 2) measurement locations were 15.9 cm (±0.05 cm) and 29.8 cm (±0.05 cm) downstream from the nozzle exit, respectively. The half-nozzle arrangement produced a nominally Mach 4.9 turbulent boundary layer flow along the test section floor. The total pressure in the settling chamber was $P_0 = 2345$ kPa (±20 kPa) and the stagnation temperature was $T_0 = 380$ K (±5 K). These were monitored using an Endevco Model 8540

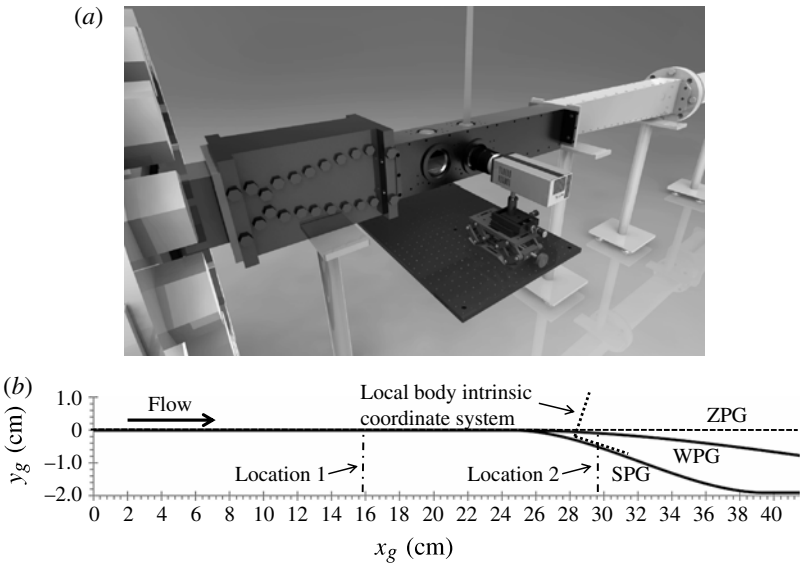

FIGURE 1. Schematic of the experimental arrangement. (*a*) Schematic of the experimental set-up (flow direction is to the right, whereas the laser light sheet entered from the top). (*b*) Wall geometry of the favourable pressure gradient models (ZPG, WPG, SPG). Locations 1 and 2 depict measurement locations, 15.9 and 29.8 cm downstream of the nozzle exit plane, respectively. Note the exaggerated ordinate for clarity.

Model	M_∞	δ (mm)	T_{aw} (K)	U_τ (m s^{-1})	I_p	I_ϕ	β	Re_θ	$Re_{\delta 2}$
ZPG[a]	4.9	7.8	342[c]	39	0.0[d]	0.0	0.07[d]	43 000	9000
WPG[b]	4.9	10.0	320	37	−0.08	0.03	−0.3	55 000	11 000
SPG[b]	4.9	13.4	317	39	−0.49	0.18	−1.0	74 000	13 000

TABLE 1. Flow conditions: [a]measurement location 1; [b]measurement location 2 (see the text for details); [c]recent temperature-sensitive-paint measurements have shown the wall temperature to be slightly below adiabatic (∼321 K) (see Humble *et al.* 2012); [d]estimated from boundary layer growth within the test section.

0–3048 kPa high-temperature pressure transducer (±0.75 % manufacturer's quoted uncertainty) and an Omega JQSS thermocouple, amplified by an OMNI AMP-IV thermocouple amplifier, respectively. Static pressure within the test section was measured with an MKS Series 902 0–101 kPa pressure transducer (±1 % manufacturer's quoted uncertainty), and was located on the sidewall approximately 5 cm downstream of the nozzle exit. Signals from the thermocouple and pressure transducers were transmitted to a National Instruments SC-2345 signal conditioner block, and collected by a National Instruments 6036E data acquisition board.

Three pressure gradient models were considered in the present study: ZPG, weak pressure gradient (WPG) and strong pressure gradient (SPG). The flow conditions are listed in table 1. Here M_∞ is the upstream (pre-expansion) free stream Mach number. The boundary layer thicknesses were estimated from the measured velocity profiles based on a 99 % free stream velocity U_∞ criterion. Because of the relatively

	X_1 (cm)	X_2 (cm)	A	B
WPG	24.54	63.54	6.42×10^{-5}	-3.757×10^{-3}
SPG	24.54	39.64	1.107×10^{-3}	-2.507×10^{-2}

TABLE 2. Model geometry and pressure gradient parameters.

small field of view and boundary layer growth, it was relatively straightforward to calculate the boundary layer thickness. The wall shear-stress values were estimated by considering the slope of the logarithmic layer within the boundary layer via the van Driest II transformation. The Clauser (1956) equilibrium pressure gradient parameter, $\beta = (\mathrm{d}p/\mathrm{d}x)(\delta^*/\tau_w)$, was deduced, where δ^* is the (incompressible) displacement thickness and τ_w is the wall shear stress. The pressure gradients within the field of views were determined from measured wall pressures obtained from multiple wall pressure taps along each model. The incompressible momentum thickness Reynolds numbers are given by $Re_\theta = \rho_e U_e \theta/\mu_e$ and $Re_{\delta 2} = \rho_e U_e \theta/\mu_w$, respectively, where ρ is the density, θ is the (incompressible) momentum thickness and μ is the dynamic viscosity.

2.2. *Curvature-driven favourable pressure gradients*

The streamline curvature-driven pressure gradient wind-tunnel models, sketched in figure 1(*b*), were designed to produce significant extra strain rates on boundary layers of interest to an ongoing campaign to study the response of compressible turbulent boundary layers to global mechanical distortions (see Ekoto *et al.* (2009) for further details). The curved walls were machined to match the following polynomial profile: $y = A\,(X - X_1)^3 + B\,(X - X_1)^2$, where A and B are the polynomial coefficients, $X = 0$ indicates the location of the nozzle exit and X_1 is the axial location where the curvature begins. Table 2 lists the geometric parameters, as well as X_2, the axial location where the wall curvature ends.

2.3. *Particle image velocimetry*

Two-component planar PIV was utilized to obtain the velocity vector fields. The flow was seeded with dioctyl phthalate (DOP) using a TSI, Inc. (2003) model 9306 six-jet atomizer, which created particles with an average diameter of approximately 250 nm (manufacturer's specification). The atomizer was housed inside a seeder box and was pressurized above the tunnel settling chamber pressure. The seeder box was then connected to a strut between the wind tunnel settling chamber and nozzle contraction using 1.27 cm (0.5 in) aluminum tubing. The strut was located along the centreline near the nozzle floor to concentrate the seeding within the region of interest.

The ability of the particles to faithfully track the flow is an important issue in high-speed flow. The Stokes number, $St = \tau_p/\tau_{flow}$, may be used to characterize the fidelity of the tracer particles, where τ_p is the particle response time and τ_{flow} is a characteristic flow time scale. For accurate flow tracking at the time scale of τ_{flow}, it is a necessary condition that $St \ll 1$. The temporal response of the present particles was estimated assuming Stokes' flow by $\tau_p = (d_p^2 \rho_p/18\mu)(1 + 2.76Kn_p)$, where the subscript p represents the seed particle's properties and $Kn_p = M/Re_p\sqrt{\gamma\pi/2} \approx 0.54$ is the particle Knudsen number, based on the free stream conditions and the manufacturer's specified particle diameter, assuming monodispersion (see Raffel *et al.* 2007). Assuming a characteristic flow time scale, $\tau_{flow} = \delta/U_\infty$, then $St \sim 0.07$. The particles are therefore

Model	Measurement location	Resolution (pixels mm^{-1})	Field of view (mm × mm)	Final window size (%δ)	Camera rotation (clockwise, deg.)
ZPG	1	78.5	20.4 × 15.3	10.5 × 10.5	0.0
WPG	2	65.1	24.6 × 18.4	9.8 × 9.8	1.6
SPG	2	65.2	24.6 × 18.4	7.3 × 7.3	10.3

TABLE 3. PIV measurement parameters.

considered to accurately track the flow, at least at the time scale of τ_{flow}. However, because the above Stokes formula is valid only for solid spheres, it must be modified for the present droplets due to the different boundary condition. This results in a drag coefficient, C_d, that is 2/3 the Stokes flow value for solid spheres (see Mei 1996), meaning that the time constant is 3/2 longer, giving $St \sim 0.11$. Naturally, to track at smaller time scales, typically associated with smaller-scale structures, then this condition will no longer hold. Hence, the present observations may be biased toward larger scales. As such, the present study focuses primarily on the large-scale processes away from the near-wall region (see § 2.4). The agreement between the present data and the literature in figure 2(*a*,*b*) indicate that the particle tracking is acceptable down to at least $y/\delta = 0.2$ before significant issues are encountered. In addition, it should be noted that the particles may not be monodispersed, and their response time was not independently verified. Recently, however, Ecker *et al.* (2012) experimentally investigated the particle step response of DOP in a Mach 2 facility and demonstrated acceptable particle response for DOP seed up to 0.65 μm agglomeration. Therefore, the theoretical estimate of the present study appears acceptable.

The flow was illuminated by a dual port/dual head variable frequency New-Wave Solo 120 XT PIV laser system. The system provided a stable, high-energy light pulse at 532 nm with a maximum energy output of 120 mJ per head with a pulse width of 4 ns (±1 ns). Beam splitting optics were placed at the outlets of the two lasers, in order to align the beams into a single path. A cylindrical lens was positioned in the beam path to create a uniform laser sheet that was approximately 50 mm wide and 0.5 mm thick. Knife-edge filters were used to remove the low-energy fringes and to provide a near top-hat light intensity distribution within the test section. The acrylic tunnel floor models also helped reduce laser light reflections at the wall.

The particle images were recorded with a 14-bit Cooke Corporation PCO 1600 charge-coupled device (CCD) camera, with a 1600 × 1200 pixel resolution. The camera was equipped with a Nikon AF Micro-NIKKOR 60 mm $f/2.8D$ lens. The f-number was set to 5.6 to optimize the diffraction spot size and avoid peak-locking. The camera was rotated 1.6 and 10.3° for the WPG and SPG models, respectively, to keep the field of view parallel to the local model surface. Image acquisition was carried out using Cooke CamWare software (v. 2.19, build 0141). The timing of each laser pulse and the camera was driven by a Quantum Composers, Inc. Model 9618 Digital Delay-Pulse Generator. A summary of the PIV measurement parameters for each pressure gradient model is given in table 3.

Velocity vector fields were obtained using the dPIV 32-bit analysis code version 2.1 from Innovative Scientific Solutions, Inc. (2005). A two-step adaptive correlation calculation was carried out using successive square interrogation window sizes of 128 × 128 and 64 × 64 pixels with a 50 % overlap factor. The final interrogation window sizes, as a percentage of the respective boundary layer heights are shown in

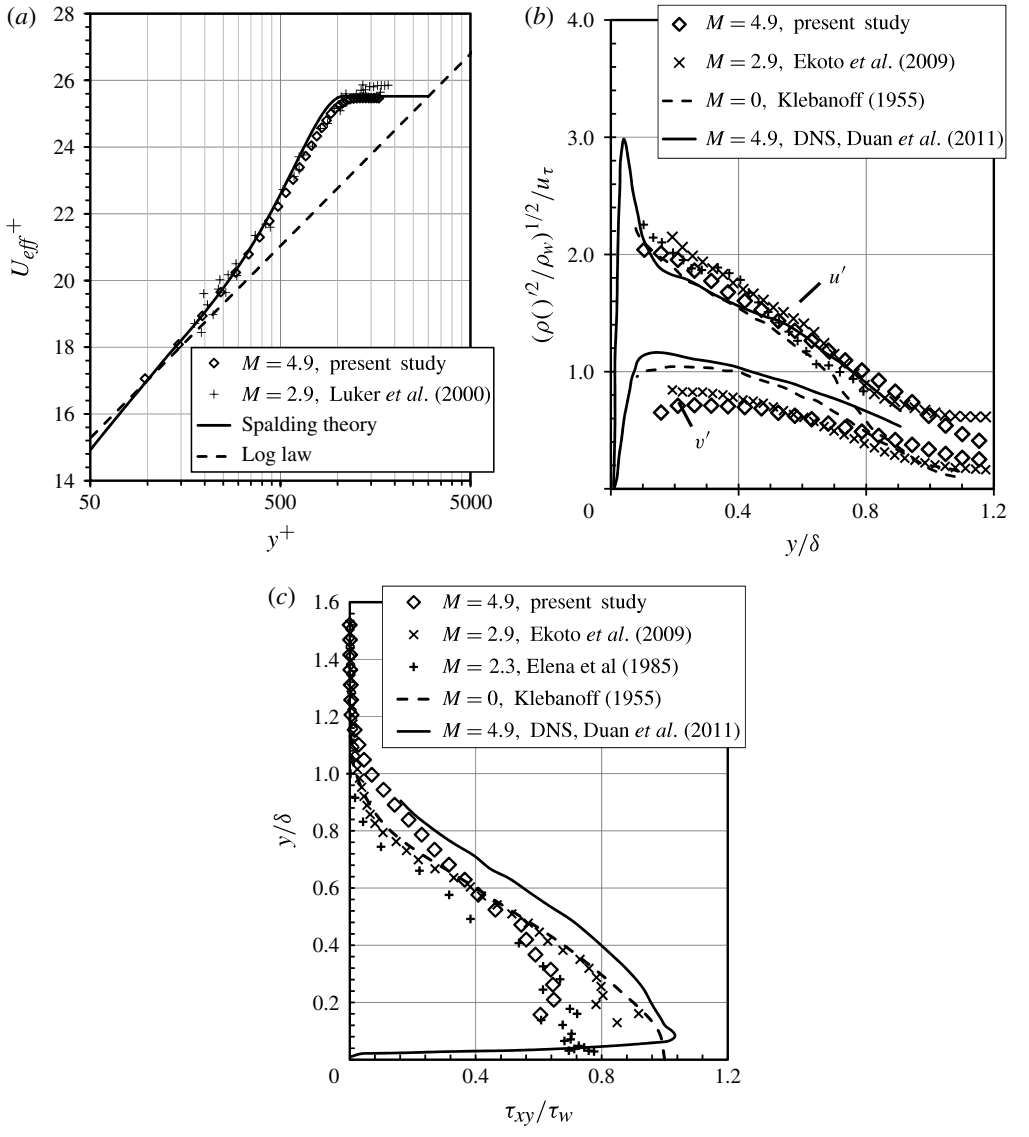

FIGURE 2. Incoming boundary layer properties (location 1). (*a*) Mean velocity with inner scaling. The solid line shows the composite formula of Spalding (1961), the dashed line shows the log law. (*b*) Turbulence intensities using Morkovin's scaling. (*c*) Reynolds shear stress distribution. The dashed line shows the incompressible results of Klebanoff (1955).

table 3. In addition, correlation multiplication (50 % overlap) and consistency filtering was activated on all four maps adjacent to the centre map to minimize spurious correlation peaks. Statistical quantities and all subsequent analyses were computed using in-house computer codes written in FORTRAN and MATLAB. Spurious vectors determined by the filters were removed. At least 90 % of the vectors were determined to be valid throughout most of the boundary layer, although closer to the wall ($y/\delta < 0.3$), the number of valid vectors decreased to 70–80 %. An ensemble-average filter of three standard deviations was utilized for the time-averaged statistics.

Variable	Uncertainty (%)
ε_x/L_{ZPG}, ε_y/L_{ZPG}	3.7
$\varepsilon_\delta/\delta_{ZPG}$	3.5
ε_U/U_∞	0.3
$\varepsilon_{\overline{u'u'}}/\overline{u'u'}_{r.m.s.}$, $\varepsilon_{\overline{v'v'}}/\overline{v'v'}_{r.m.s.}$	5.5
$\varepsilon_{\overline{u'v'}}/\overline{u'v'}_{r.m.s.}$	9.9
$\varepsilon_{\mathrm{d}\overline{u}/\mathrm{d}x}/\ (\mathrm{d}\overline{u}/\mathrm{d}x)_{r.m.s.}$, $\varepsilon_{\mathrm{d}\overline{u}/\mathrm{d}y}/\ (\mathrm{d}\overline{u}/\mathrm{d}y)_{r.m.s.}$	2.0

TABLE 4. Estimated measurement uncertainties.

In the present study, 3000 vector fields were acquired at each measurement location. The measurement grid consisted of 49×34 data points, with a (final) vector spacing of 0.40, 0.49 and 0.49 mm for the ZPG, WPG and SPG models, respectively. In addition, the free stream pixel displacements as a fraction of the final interrogation window sizes were approximately 0.5, 0.4 and 0.4 for the ZPG, WPG and SPG cases, respectively. Finally, profile data were streamwise-averaged over approximately the centre 20 % (4–5 mm) of the field of view to aid statistical convergence, although this did not change the conclusions drawn. For example, the axial averaging accounted for a maximum normalized difference of only 4×10^{-6} for the most sensitive statistic, $\overline{u'v'}$ (SPG).

2.4. *Measurement uncertainties*

Measurement uncertainties for the present study are summarized in table 4 and were accumulated with a Euclidean (L_2) norm. The axial and transverse position uncertainty within the camera field of view were estimated to be within 2 pixels ($\sim$0.03 mm) on the camera array, and were normalized using the ZPG final interrogation window size ($L_{ZPG} \sim 0.82$ mm). Boundary layer thickness uncertainty accounted for the uncertainties in position and velocity, where the sensitivity to the velocity uncertainty was estimated with a 1/7th power law. To estimate the uncertainty in the statistical quantities, a 95 % confidence interval was used, determined assuming a distribution of 3000 samples (see Benedict & Gould (1996) for further details). Because the magnitude of the transverse velocity was comparatively small, the magnitude of the transverse velocity uncertainty was taken to be the same as the axial velocity. Note that the tabulated fluctuating velocity correlation uncertainty is only for $y/\delta > 0.1$; nearer the wall, the uncertainties were considered unreliable due to low seeding density and appreciable laser light reflections. The velocity gradient uncertainty was calculated using a combination of the uncertainties in spatial position and mean velocity measurements. The spatial difference uncertainty only accounted for the conversion error from the physical length scale to the PIV image pixels. The mean velocity uncertainty included the value listed in table 4. Owing to the limitations of PIV to capture small-scale effects in these flows, the present observations may be biased toward larger scales.

2.5. *Flow-field two-dimensionality*

In order to assess the flow two-dimensionality of the incoming boundary layer, PIV measurements were acquired at three spanwise locations ($z/\delta = +1.6, 0.0, -1.6$, where $z/\delta = 0$ is the centreline) at the upstream measurement location (location 1). The PIV data were limited to this spanwise range due to the finite size of the seeding volume that could be achieved. The spanwise velocity profiles showed that the flow was

uniform across the measured region to within approximately 0.5 % U_e, where U_e is the edge boundary layer velocity. These data indicate that the flow is symmetric about the centreline, with minimal change within the spanwise region considered. Accordingly, it is reasonable to assume that the flow statistics are nominally homogeneous along the centreline. Efforts currently are underway to assess the spanwise organization of the expansion region.

3. Results

3.1. *Incoming boundary layer*

As the prelude to the main results, the incoming boundary layer is characterized in detail. Van Driest II scaling has proven effective in collapsing supersonic mean boundary layer velocity profiles (Van Driest 1956). The ZPG mean velocity profiles, utilizing this van Driest II scaling, are plotted with inner variables in figure 2(*a*). Included are the Mach 2.9, $Re_{\delta 2} = 9000$ results of Luker *et al.* (2000). The density variation was determined using the Crocco–Busemann relation, with a constant recovery factor, $r = 0.89$. The solid line is Spalding's (1961) composite law of the wall, in combination with Coles's (1956) wake function with the wake parameter (Π) set to 0.55. The dashed line shows the logarithmic layer equation, $u^+ = \kappa^{-1} \ln y^+ + B$, where κ is the von Kármán constant and B is the intercept. The wall shear stress in each case was determined using a slope in the logarithmic region as $\kappa = 0.4$ and $B = 5.5$ as described in the next paragraph.

The estimation procedures for the friction velocity are similar to those of Lewis, Gran & Kubota (1973), where here the fits were limited to the log region. The resulting friction velocities are summarized in table 1. Referring to figure 2(*a*), it is clear that only a few points are within the logarithmic region. Hence, the ZPG data were compared with the van Driest II theory (Van Driest 1956) described in Hopkins (1972), where the incompressible skin friction relation, $C_{f,inc} = 0.456 {Re_\delta}^{-1/4}$, of Schultz-Grunow (1940) as shown in Schetz (1993) was used. Specifically, $C_f = C_{f,inc}(F_{th} Re_\delta)/F_c$, where $F_{th} = \mu_e/\mu_w$, $F_c = (T_{aw} - 1)/\left(\sin^{-1} A + \sin^{-1} B\right)^2$, $A = B_1^2/B_3$, $B = B_2/B_3$, $B_1 = \sqrt{(T_{aw} - T_e)/T_w}$, $B_2 = T_{aw}/T_w - 1$ and $B_3 = \sqrt{4B_1^2 + B_2^2}$. The resulting friction velocity was within 2 % of that in table 1. This agreement is considered fortuitous as the van Driest II theory is generally accepted to be accurate to within 10 % (see Bradshaw 1977). It has also been reported that B and κ depend on pressure gradient (McDonald 1968; Nagib & Chauhan 2008). Following McDonald, the relevant parameter is $\alpha_0 = (\nu/\rho u_\tau^3)(\partial p/\partial x)$, which is equal to $\nu/(u_\tau \delta)\beta$. For the present SPG flow, α_0 peaks at -0.0016, which suggests a negligible effect on the law-of-the-wall constants.

Morkovin (1961) scaling removes, to a certain extent, compressibility effects from wall-bounded turbulence data, whereby the mean density variation across the boundary layer is taken into account. The present ZPG velocity fluctuation data are compared with previous experimental studies ranging from $M = 0$ to 2.9 in figure 2(*b*,*c*), where the friction velocity follows from the previous paragraph. Also shown are the $M = 4.9$ direct numerical simulation (DNS) data of Duan & Martin (2011). The present turbulence intensity data, in figure 2(*b*), agree with expected trends to within the scatter of the data. For the Reynolds shear stress comparison in figure 2(*c*), the scatter among the studies is considerably larger, and the present data tend toward under prediction. A primary difficulty with this comparison is the lack of a direct measurement of the wall shear stress for the present study. However, it appears that both the van Driest II and Morkovin's scaling, derived based on the weak

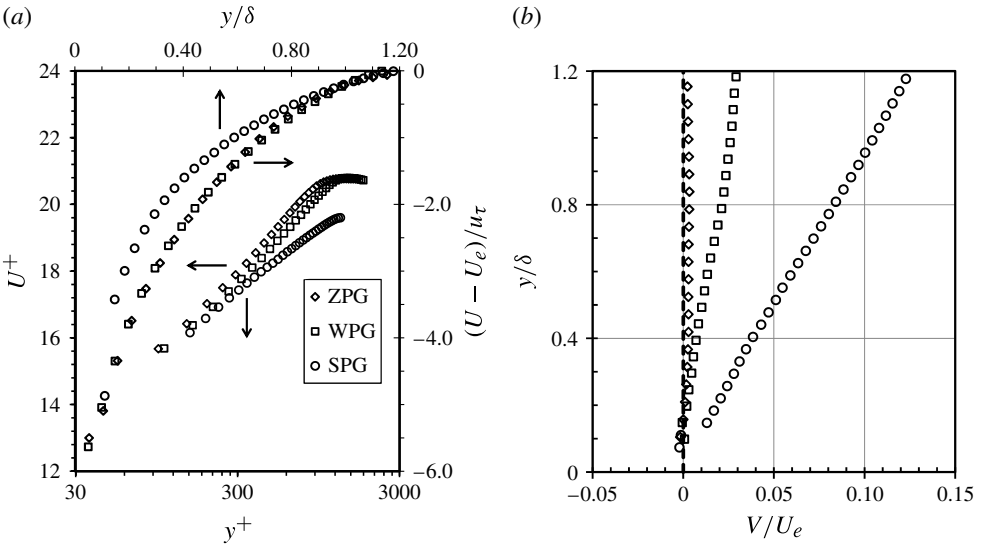

FIGURE 3. Mean velocity distributions. Arrows indicate appropriate axes: (*a*) axial velocity (inner and outer scaling); (*b*) transverse velocity.

compressibility hypothesis, remain valid for the present hypersonic boundary layer, consistent with the finding of Duan & Martin (2011). The present ZPG data, which were acquired $\sim 20\delta$ downstream of the nozzle exit, are considered representative of a ZPG flat plate boundary layer, and consequently provide a suitable basis for the following favourable pressure gradient comparisons.

3.2. *Mean velocity and strain rates*

Velocity profile data, with both inner and outer scaling, for the three pressure gradients are summarized in figure 3(*a*). The inner variable scaling is plotted on the left and bottom axes, whereas the defect law scaling is plotted on the upper and right axes. Density scaling was not employed as the data were all acquired at nominally the same Mach number. For all three test cases, the results show a linear collapse for $y^+ < 200$. For $y^+ > 200$, the profiles show the expected reduction in the wake function as the favourable pressure gradient strength increases (see, e.g., White 2006). With defect scaling, the ZPG and WPG boundary layer profiles are similar, although the WPG has a slightly lower defect in the outer half of the boundary layer. As anticipated, the SPG boundary layer profile has a smaller defect over most of the boundary layer, indicating a fuller velocity profile. This was also observed by Luker *et al.* (2000). The scaling of Zagarola & Smits (1998) showed the same qualitative behaviour as the classical scaling shown in figure 3(*a*). For completeness, the transverse velocity profiles are plotted in figure 3(*b*); these data show a near linear increase in transverse velocity with distance from the wall.

The mean strain rates were computed using central differencing and are summarized in figure 4. The principal strain rate $[S_{xy} = (\partial U/\partial y + \partial V/\partial x)/2]$ and (in plane) bulk dilatation $(\partial U/\partial x + \partial V/\partial y)$ for the ZPG and SPG are compared in figure 4(*a*). Notably, in the outer 75 % of the boundary layer, the principal strain rate for the SPG flow is substantially reduced, by ~ 0.05 in the units plotted. For the WPG data, however, the

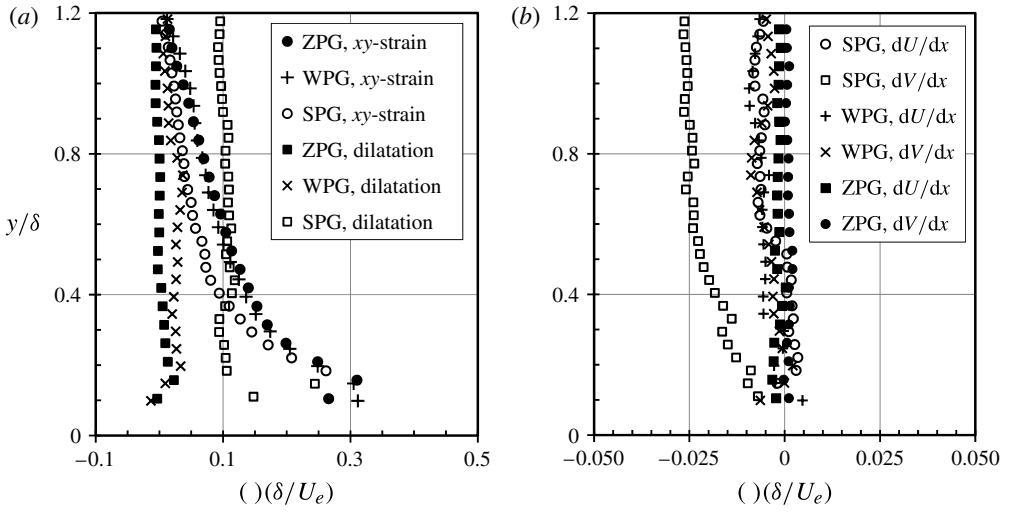

FIGURE 4. Mean strain rate profiles: (*a*) S_{xy} and $\boldsymbol{\nabla}\cdot\boldsymbol{V}$; (*b*) axial strain rates.

reduction is more subtle, yet systematic, at ∼0.01. For $y/\delta < 0.25$, the principal strain rates are similar for all three cases.

A second important feature, shown in figure 4(*a*), is the magnitude of the SPG bulk dilatation, which exceeds the principal strain rate in the outer 60 % of the boundary layer by approximately 0.04 on average. This suggests that bulk dilatation is a dominant extra strain in the outer part of the boundary layer, consistent with the work of others (see, e.g., Dussauge & Gaviglio 1987). The WPG results are qualitatively similar to the SPG in the outer region, where the dilatation is nominally 0.04. The axial gradients, $\mathrm{d}U/\mathrm{d}x$ and $\mathrm{d}V/\mathrm{d}x$, are shown in figure 4(*b*), and are significantly smaller than the transverse gradients. The only substantial gradient is $\mathrm{d}V/\mathrm{d}x$ for the SPG flow, which increases in magnitude across the boundary layer to −0.03 (in the units plotted). Luker *et al.* (2000) found that the production associated with this gradient was significant enough to change the sign in the overall production.

Examination of the individual strain rates reveals that $\mathrm{d}V/\mathrm{d}y$ accounts for most of the SPG bulk dilation, where the magnitude of $(\mathrm{d}U/\mathrm{d}x)/(\mathrm{d}V/\mathrm{d}y)$ is nominally 5–10 %. A similar ratio was also reported by Ekoto *et al.* (2009). The contributions for the WPG case are more balanced, where the magnitude of $(\mathrm{d}U/\mathrm{d}x)/(\mathrm{d}V/\mathrm{d}y)$ is nominally 10–50 %. Because $\mathrm{d}U/\mathrm{d}x$ remains quite similar for both the WPG and SPG cases (cf. Figure 4*b*), then it can be deduced that it is the $\mathrm{d}V/\mathrm{d}y$ term that is sensitive to the pressure gradient. Furthermore, because the transverse velocity varies almost linearly with distance from the wall; then $\mathrm{d}V/\mathrm{d}y$ is constant and explains why the bulk dilatation is practically constant throughout almost all of the boundary layer that can be resolved. We shall see the significance of this term in the Reynolds stress transport mechanisms in § 4.

3.3. *Reynolds stresses*

The Reynolds stresses for the ZPG, WPG and SPG cases are presented in figure 5(*a–c*). These data summarize the response of the turbulence within the boundary layer to the streamline curvature-driven pressure gradients. Although the results are presented in a wall-normal coordinate system, the role of the coordinate

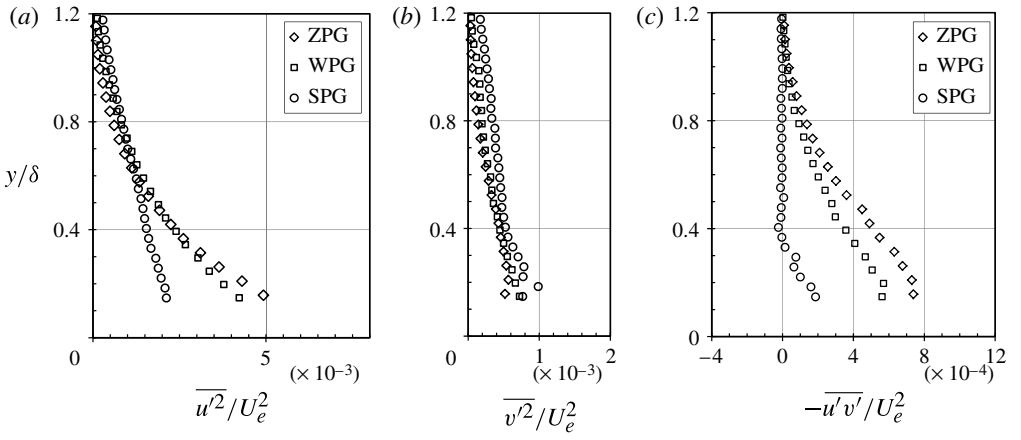

FIGURE 5. Reynolds stress profiles: (*a*) axial component; (*b*) transverse component; (*c*) shear component.

system on the results was examined by transforming the ZPG data from the upstream coordinate system to the downstream SPG body intrinsic system. For the WPG, the rotation was only 1.6°, and negligible. Even though for the SPG the rotation was 10.3°, the axial and transverse stresses showed only a modest dependency, with a peak non-dimensional change of approximately 3×10^{-4} (in the units plotted). The Reynolds shear stress, however, showed a relatively large reduction of approximately 85 %.

The distribution of the axial turbulence stress within the boundary is given in figure 5(*a*) for the various test cases considered. A systematic reduction in the axial stress with increasing favourable pressure gradient strength can be observed in the lower half of the boundary layer. For the SPG case in particular, there is a significant reduction in axial stress for $y/\delta < 0.5$. A slight increase in the outer region is observed for the pressure gradient cases, which may be a result of increased velocity fluctuation scales due to bulk dilatation (see § 4). Nevertheless, the general trends are in qualitative agreement with the Mach 2.9 data of Luker *et al.* (2000) and Ekoto *et al.* (2009).

The transverse turbulence stresses are presented in figure 5(*b*). They show a systematic increase across the boundary layer as the pressure gradient strength increases, but they remain substantially lower than the axial turbulent stresses. Again, the present SPG trends are similar to those of Ekoto *et al.* (2009) and Luker *et al.* (2000).

The Reynolds shear stress profiles are depicted in figure 5(*c*). The expected systematic decrease with increasing pressure gradient strength is observed, with the SPG turbulent shear stress showing a dramatic reduction. For $y/\delta > 0.4$, the SPG Reynolds shear stress is practically zero, and even slightly negative. These slightly negative values are an important result: they indicate that there may be decaying turbulent motions in this region of the boundary layer, and that the mean flow may be extracting energy from the turbulent flow (see also Arnette *et al.* (1998)). This is also consistent with the fuller velocity profile in figure 3(*a*). Similar profiles were obtained at Mach 2.9 by Arnette *et al.* (1998) and Luker *et al.* (2000), although Ekoto *et al.* (2009) did not observe a sign change. Referring back to figure 4(*a*), it is interesting to note that the Reynolds stress is practically zero in the same region of the boundary

layer where bulk dilation (in this case essentially $\mathrm{d}V/\mathrm{d}y$) exceeds the principal strain rate ($\mathrm{d}U/\mathrm{d}y$).

3.4. *Turbulence structure*

3.4.1. *Reynolds stress quadrant decomposition*

The effects of the favourable pressure gradients on the preferred orientation of turbulent events within the boundary layer may be examined using the quadrant decomposition technique of Lu & Willmarth (1973). This method has been widely implemented to study the degree of reoccurrence and strength of dynamic boundary layer events, such as eddy ejections and sweeps (see e.g. Herrin & Dutton 1997; Adrian, Meinhart & Tomkins 2000; Panigrahi, Schroeder & Kompenhans 2008; Nolan, Walsh & McEligot 2010). The velocity fluctuations measured from the PIV data are used for the quadrant decomposition technique by separating the data into four possible quadrants: Q1 'outward interaction' events, $u' > 0, v' > 0$; Q2 'ejection' events, $u' < 0$, $v' > 0$; Q3 'inward interaction' events, $u' < 0$, $v' < 0$; and Q4 'sweep' events, $u' > 0, v' < 0$, where u' and v' are instantaneous velocity fluctuations about the mean velocity.

In addition, to characterize the orientation of the velocity fluctuations, an instantaneous shear angle, $\Psi = \tan^{-1}(v'/u')$, is defined. The quadrant decomposition was carried out at various wall-normal locations for each test case. From these results, discrete probability density functions (p.d.f.s) may be generated, which indicate the relative probably of Ψ_i falling within a certain range of angles. The average contribution to the velocity correlation for each quadrant was calculated from

$$\overline{(u'v')_i} = \frac{1}{N}\sum_{n=1}^{N}[(u'v')_i]_n, \quad i = 1 \ldots 4, \tag{3.1}$$

where

$$\sum_{i=1}^{4}\overline{(u'v')_i} = \overline{u'v'}. \tag{3.2}$$

Here, N is the number of samples, n is the current sample number and i indexes the quadrant number. Following Nolan *et al.* (2010), the quadrant contribution may be partitioned further, based on the strength of the respective motion within the flow. For this analysis, a contribution to a quadrant motion is included if $|\overline{u'v'}| > H_S|\overline{u'v'}|_{ref}$, where H_S is the so-called hole-size parameter and $|\overline{u'v'}|_{ref}$ is a constant reference shear stress value. The basic idea behind the method is that regions greater than the reference shear stress may be isolated (see figure 6). When $H_S = 0$, all contributions to the shear stress are included, and the sum of the four quadrant contributions is the total turbulent shear stress. As H_S is increased, only larger fluctuations are considered. $|\overline{u'v'}|_{ref}$ was taken as the average across the ZPG boundary layer of $u'_{rms}v'_{rms}$, which has a value of 272 $\mathrm{m^2\ s^{-2}}$.

Example quadrant decomposition results for the ZPG boundary layer at $y/\delta = 0.3$ are given in figure 6. The scatter plot shows that the Reynolds stress is predominantly a balance between Q2 and Q4 events. The shear angle p.d.f. shows a well-defined peak for the shear angle of approximately $-10°$, which indicates a consistent orientation of the velocity fluctuations about the mean flow. This organization is consistent with previous observations of large-scale turbulent structures within compressible shear layers (see e.g. Herrin & Dutton 1997). These fluctuations yield negative shear angles

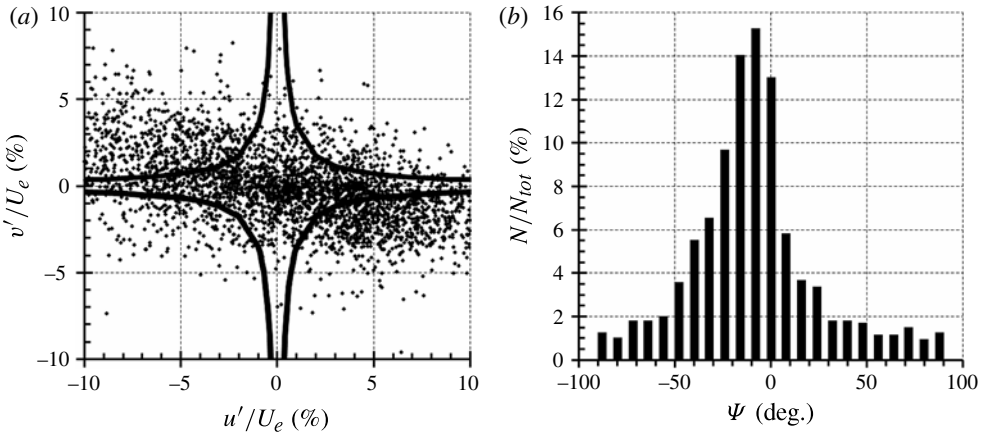

FIGURE 6. Reynolds stress quadrant decomposition results. (*a*) Scatter plot showing H_S boundary. When $H_S = 0$, all contributions to the shear stress are included, and the sum of the four quadrant contributions is the total turbulent shear stress. As H_S is increased, only larger fluctuations are considered. (*b*) Shear angle. ZPG boundary layer, $y/\delta = 0.3$.

which correspond to Q2 and Q4 events. Similar plots were acquired for locations across the boundary layer, and it was found that the magnitude of the velocity fluctuations decreases significantly with distance from the wall, with a significant grouping near the origin. Yet the instantaneous shear angle appears to be relatively insensitive to wall-normal location.

The corresponding analyses for the WPG case yield velocity fluctuations of the same order as the ZPG; however, the structures are less clearly aligned along the ZPG preferential direction. It is likely that the WPG begins to reorient some of the coherent flow structures within the boundary layer. The dominant shear angle, however, is still approximately $-10°$ because the WPG has only a modest wall curvature.

In contrast, the Reynolds stress quadrant decomposition analyses for the SPG exhibit slightly smaller velocity fluctuations compared with the ZPG and WPG, accompanied by a less-defined dominant shear angle at approximately 0°. This shift in preferred shear-angle orientation appears to correspond directly to the rotation of the local wall normal coordinates relative to the wind tunnel axes (10.6°). The velocity fluctuations from the present data, when plotted in this representation, show less organization along any particular angle, suggesting that they become less correlated with each other. This is consistent with a decrease in Reynolds shear stress, and the notion that the turbulent structures are reorganized with favourable pressure gradient.

Wall-normal profiles of the quadrant averaged Reynolds shear stresses were extracted from the quadrant analysis for each test case to further characterize the turbulence structure. The normalized Reynolds stress components, as well as the contribution of quadrant events to the Reynolds shear stress are presented in figure 7. Considering first the ZPG boundary layer, we can see in figure 7(*a*) that the Q2 and Q4 events typically have the largest normalized values. These are associated with ejection and sweep events, respectively, which are known to be dominant processes in incompressible turbulent boundary layers (see, e.g., Adrian *et al.* 2000). The overall observed trends are consistent with low-speed data reported by Lu & Willmarth (1973), Raupach (1981) and Krogstad & Skare (1995). For example, the present ZPG data are compared with the results of Krogstad & Skare (1995) ($U_e = 24.9$ m s^{-1},

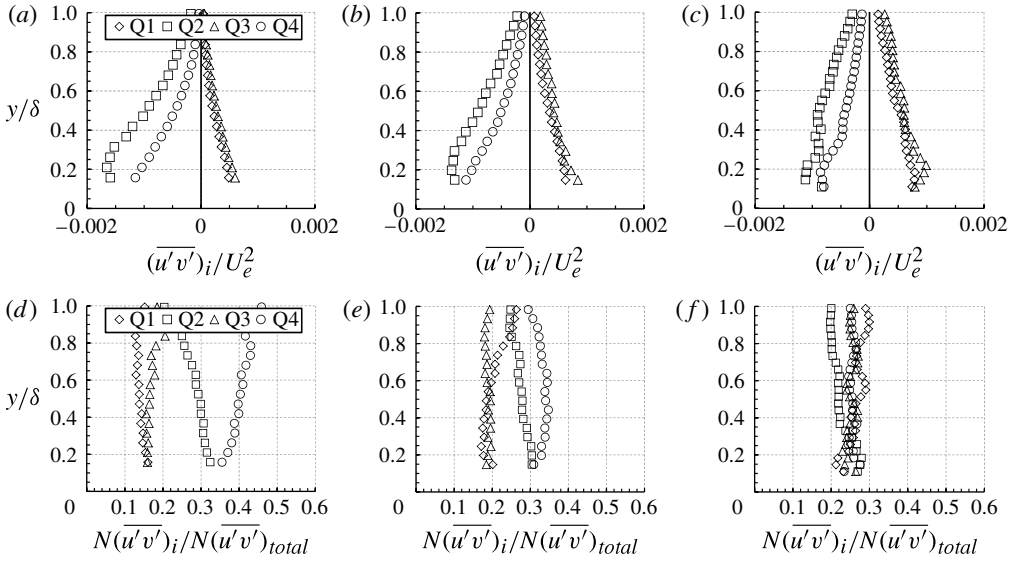

FIGURE 7. Quadrant decomposition analysis. (*a–c*) Reynolds stresses normalized by $U_e{}^2$: (*a*) ZPG; (*b*) WPG; (*c*) SPG. (*d–f*) Reynolds stress contributions ($H_s = 0$).

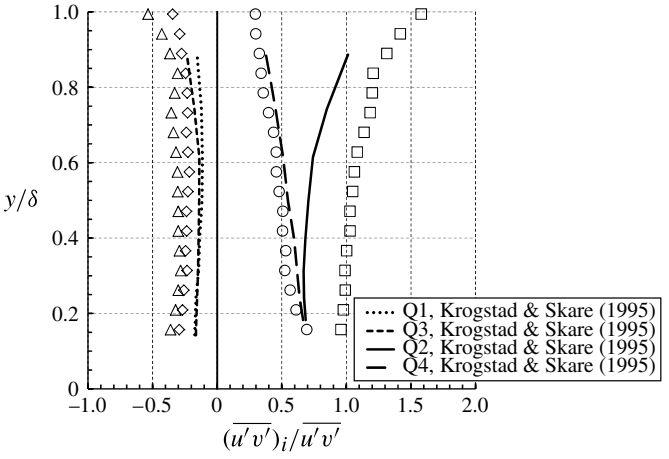

FIGURE 8. Contributions to $\overline{u'v'}$ from Reynolds stress quadrants. Lines are the ZPG results of Krogstad & Skare (1995) ($U_e = 24.9$ m s^{-1}, $Re_\theta = 12\,600$). Symbols for present study as shown in figure 7(*a*).

$Re_\theta = 12\,600$) in figure 8, where the trends of the four quadrant components are similar. It therefore appears that the present ZPG boundary layer shares the Q2- and Q4-dominated turbulence dynamics of its incompressible counterpart. One notable difference for reasons presently unknown is that, in the present study, the relative contribution of the Q2 ejection events is significantly higher than for the incompressible data.

The effect of pressure gradient on the quadrant data are presented in figure 7(*b*,*c*). Most notable is an observed reduction in the Q2 and Q4 events throughout the

boundary layer. The decrease in Q2 is particularly apparent closer to the wall for the SPG. Normalizing the quadrant events by the total number of events, $N\,(\overline{u'v'})_i\,/N\,(\overline{u'v'})_{total}$, is more revealing. Since the physical interpretation of Q4 events is that they are associated with fluid entrainment into the boundary layer, whereas Q2 events represent ejections of relatively low-velocity fluid into higher regions of the boundary layer, figure 7(*d*) is consistent with the idea that turbulence production mainly takes place nearer the wall, whereas entrainment processes occur in the outer part of the boundary layer, much like in incompressible boundary layers.

The data in figure 7(*e*,*f*) show that as the favourable pressure gradient strength increases, the relative differences between the quadrant contributions decreases. In particular, very little preferential quadrant mode selection is observed for the SPG case throughout most of the boundary layer. The number of Q2 and Q4 events is reduced, and essentially redistributed to Q1 and Q3 events. This suggests that the quadrant mechanisms associated with fluid entrainment from the free stream, as well as the ejection of low-velocity fluid near the wall, are no longer dominant, as presently observed in the PIV plane. This is consistent with the idea that favourable pressure gradients have a stabilizing influence on the boundary layer, in the sense that the boundary layer is losing its ability to entrain free stream fluid and transport it towards the wall. This is also consistent with the observations that the onset of intermittency moves closer to the boundary layer edge and decreases in extent with increasing favourable pressure gradient (see Humble *et al.* 2012). Luker *et al.* (2000) also observed that the favourable pressure gradient resulted in increased intermittency, which was interpreted to indicate that the large-scale structures were disintegrating into smaller ones. Additional quadrant events involving the out-of-plane motions are presently unknown.

It is also instructive to consider contributions from only relatively high-intensity quadrant events within the boundary layer, as shown in figure 9. The relative significance of the large-scale motions can be seen by comparing the cases when $H_s = 0$ in figure 7(*d–f*) to figure 9 when $H_s > 0$. For non-zero values of H_s, the remaining probability of the Reynolds stress components are significantly lower, as one would expect. For the ZPG and WPG, the Q2 and Q4 components are only slightly reduced within the lower region of the boundary layer. This implies that larger Reynolds stress fluctuations are more prevalent in this region, compared with the outer portion of the boundary layer. For the SPG, the Reynolds stress components exhibit reduced contributions, which suggests reduced fluctuations, again consistent with others (Arnette *et al.* 1995; Luker *et al.* 2000), who maintained a weakening of the large-scale turbulence organization throughout the expansion process.

3.4.2. *Two-point spatial correlations*

To make statements regarding the response of the large-scale coherent motions to the imposed pressure gradients, two-point correlations of the fluctuating velocity components were estimated using

$$R_{u_iu_j}(\Delta x, y, y_{ref}) = \frac{\overline{u_i(x, y_{ref})u_j(x+\Delta x, y)}}{\sigma_{u_i}(y_{ref})\sigma_{u_j}(y)}, \tag{3.3}$$

where y_{ref} is the reference wall-normal location at which the correlation is computed, Δx is the in-plane streamwise separation, $\sigma_u(y_{ref})$ is the root mean square (r.m.s.) of u at y_{ref} and $\sigma_u(y)$ is the r.m.s. of u at location y. The over-bar represents an ensemble average over multiple realizations. Note that the present data enable the estimation

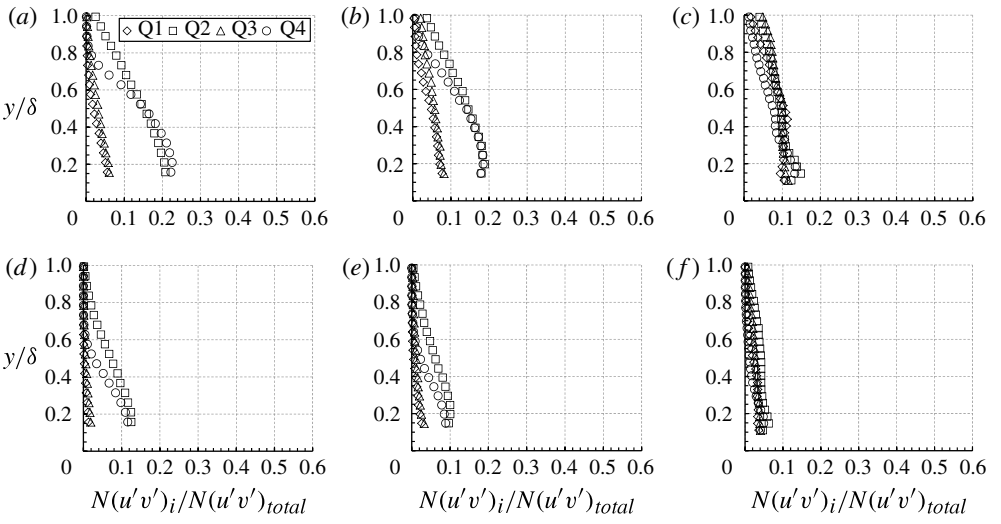

FIGURE 9. Reynolds stress component profiles from quadrant decomposition for various hole sizes: (*a–c*) $H_s = 1$; (*d–f*) $H_s = 3$. The pressure gradients are: (*a,d*) ZPG; (*b,e*) WPG; (*c,f*) SPG.

of the true two-dimensional spatial correlation function without the use of Taylor's hypothesis.

Two-point correlation maps for the axial velocity at reference locations $y/\delta = 0.3, 0.5$ and 0.8 for the ZPG, WPG and SPG are presented in figure 10. The isocontours can be seen to possess a forward-leaning elliptical distribution, consistent with numerous other previous studies of compressible boundary layers (see, e.g., Spina *et al.* 1994; Arnette *et al.* 1995; Ganapathisubramani 2007; Humble *et al.* 2012) using a variety of experimental techniques ranging from hotwire anemometry, flow visualization, to PIV. In addition, the isocorrelation values appear to exhibit a slightly greater non-dimensional spatial extent with increasing distance from the wall, suggesting larger, higher-correlated turbulent structures are present in the outer region of the boundary layer (cf. Ganapathisubramani 2007).

The effects of favourable pressure gradient on the non-dimensional spatial extent of the axial velocity two-point correlations can be seen in figure 10, where a systematic reduction is observed at all three boundary layer heights. This may be compared with the two-point spatial correlations based on flow visualization by Arnette *et al.* (1995) and Humble *et al.* (2012), who also found that the non-dimensional extent of their isocorrelations decreased somewhat with favourable gradient. As shown in figure 11 is a comparison of autocorrelations from the present study to results extracted from Arnette *et al.* (1995), who performed similar two-point correlation analyses for a Mach 3 boundary layer over a 7° expansion. As indicated, the present ZPG and SPG flow are in qualitative agreement with those of Arnette *et al.* (1995), although Arnette *et al.* (1995) interpreted their results as being consistent with the idea that the flow structures could nominally scale with the (increasing) boundary layer thickness. However, as noted by Humble *et al.* (2012), it should be stressed that the flow visualization results represent spatial correlations of light intensity (essentially representing a temperature/vorticity field) and not velocity, and so direct comparisons should be made with caution. The transverse velocity two-point correlations (R_{vv}) (not

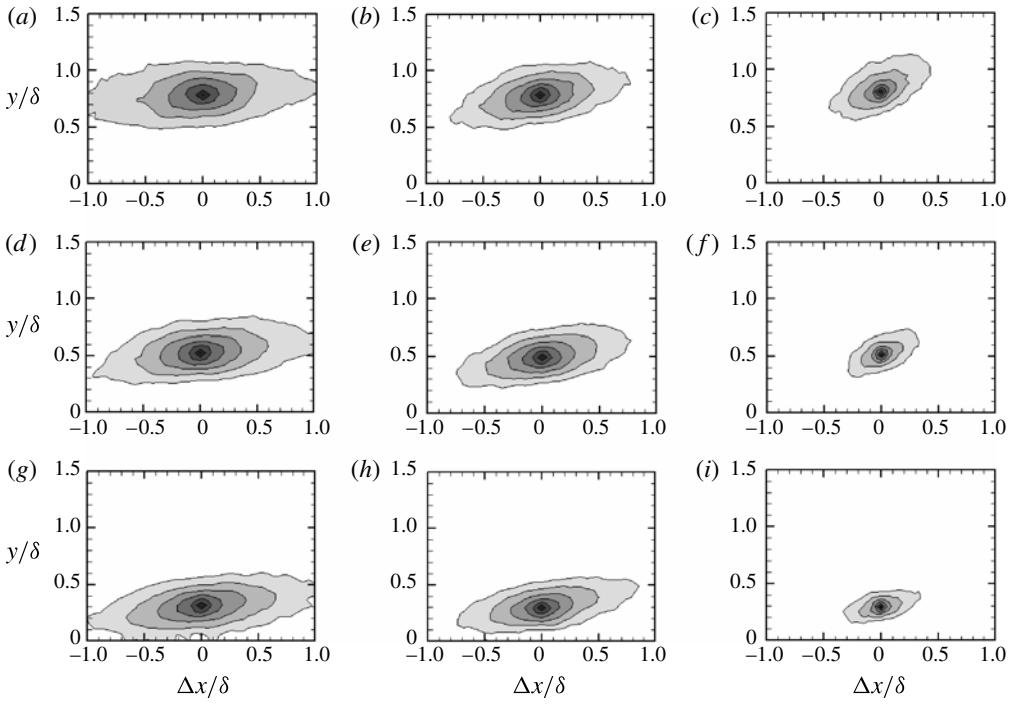

FIGURE 10. Streamwise two-point spatial maps, $R_{uu}(\Delta x, y)$. Outer (minimum) correlation value = 0.4, increase in 0.1 increments: (*a–c*) $y_{ref}/\delta = 0.8$; (*d–f*) $y_{ref}/\delta = 0.5$; (*g–i*) $y_{ref}/\delta = 0.3$. The pressure gradients are: (*a,d,g*) ZPG; (*b,e,h*) WPG; (*c,f,i*) SPG.

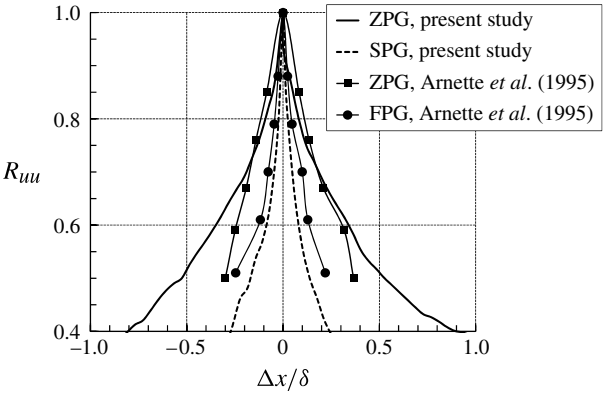

FIGURE 11. Comparison of streamwise autocorrelation $R_{uu}(\Delta x, y)$ function at $y/\delta = 0.5$ for present Mach 5 cases and Mach 3 cases of Arnette *et al.* (1995).

shown here for brevity) did not show the same elliptic trends as the *u*-component, and they extended over a much smaller non-dimensional range compared with the streamwise component.

In addition, it appears that the isocorrelations are rotated relative to the ZPG case, suggesting that the flow structures lean farther away from the wall as they negotiate

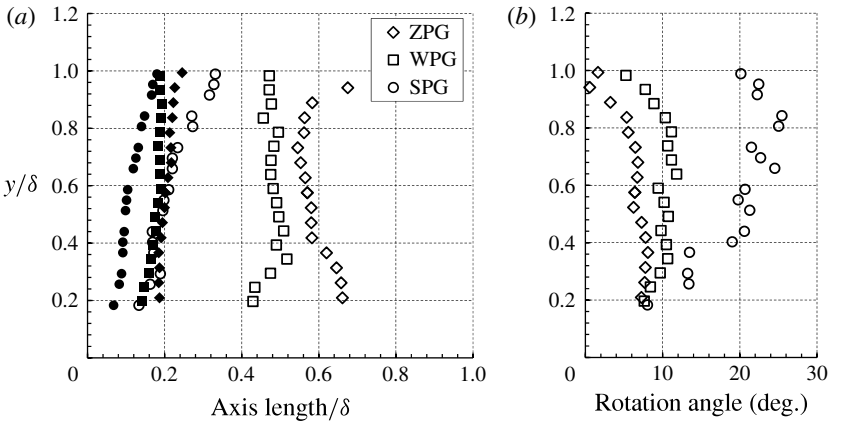

FIGURE 12. Ellipse-fitting analysis: (*a*) ellipse major axes (*open*) and minor axes (*solid*); (*b*) structure angles based on $R_{uu} = 0.5$.

the expansion. This flow structure reorientation is consistent with previous lines of inquiry. Turbulent structure reorientation through supersonic expansions was first speculated by Arnette *et al.* (1995) and recently quantified by Humble *et al.* (2012), who attributed it to the inclination and diverging nature of the expansion fan, whereby the bottom of an eddy structure is accelerated throughout the expansion fan before the top.

To quantify the change in size and orientation of the turbulent structures, an ellipse-fitting technique was performed on the isocorrelations (see Ringuette *et al.* 2009). Briefly, an ellipse is fit to the data points for a specified isocontour, and the major and minor axes lengths are recorded, as well as the inclination angle of the major axis from the wall. The results from the ellipse fitting are presented in figure 12 for $R_{uu} = 0.5$. This correlation value was chosen because the correlation sizes were small for the SPG and an elliptical contour was required in order to extract major and minor axes. Considering alternative isocorrelation values yielded similar trends for the favourable pressure gradients.

For the ZPG, the nominal rotation angle of approximately 5–8° throughout the boundary layer is in line with the results by Ringuette, Wu & Martin (2008) and Ganapathisubramani (2007), who each showed an approximate rotation angle near 10° in the lower part of their boundary layer.

The non-dimensional (major-axis) extent of the two-point correlations can be seen to decrease with increasing pressure gradient strength (see figure 12*a*), substantiating the observation of non-dimensional reduction in flow-structure size. The ellipse rotation angles presented in figure 12(*b*), confirm that the coherent structures rotate relative to the local wall direction as they negotiate the expansion. As noted by Humble *et al.* (2012), the simple rotation of the camera axis does not fully account for this flow-structure rotation, suggesting that the expansion process is partly responsible for the reorientation. The rotation angle for the WPG ranges from 8° near the wall, up to a maximum of 12° at $y/\delta = 0.6$. The structure angles for the SPG significantly increase above $y/\delta = 0.4$, which corresponds to the region of the boundary layer in which the dilatation influence is larger than the principal strain rates. It is believed that a less-elliptical correlation shape in combination with an increased $\mathrm{d}V/\mathrm{d}y$ strain rate, distorts the turbulence structures away from the wall, increasing the observed

correlation angle (figure 12*b*). It therefore appears that the expansion process modifies the orientation of the turbulent structures in different ways depending upon their location within the boundary layer: less reorientation typically occurs nearer the wall than in the (dilatation-dominated) outer part of the boundary layer.

4. Discussion: physical and Reynolds shear stress modelling

4.1. *Physical processes*

The above results, as well as the previous studies listed in § 1, show that as the flow experiences a favourable pressure gradient, the turbulence and turbulence production are reduced. With this in mind, it is expected that the large-scale flow structures are somewhat benign and begin to dissipate as they advect through the expansion. It is also expected that the turbulence being produced locally is altered due to the favourable pressure gradient, where the induced strain rate $\mathrm{d}V/\mathrm{d}y$ stretches the turbulent structures in the transverse direction leading to enhanced dissipation and perhaps eventually disintegration. The fuller velocity profiles (figure 3), reduced turbulence (figure 5), reduced correlation lengths (figure 11), redistribution of the Reynolds stresses across the quadrants (figure 7) and scales (figure 9), all support this model. Hence, given enough time (and appropriate geometry), the turbulent structures across the boundary layer may break down and eventually lead to relaminarization. These processes would be a combination of linear and nonlinear effects, and the relative time scales for the SPG flow are associated with the advection time t^* given by $tU_e/\delta \sim 6.2$, the principal strain time scale $1/(\mathrm{d}U/\mathrm{d}y)$, which ranges from $\sim$0.02 at the wall to essentially infinity in the free stream and the dilatation time scale $1/(\mathrm{d}V/\mathrm{d}y) \sim 10$. As indicated in figure 4(*a*), the principal and dilatational strain rates cross at $y/\delta \sim 0.4$. Thus, as the turbulence negotiates the expansion, two types of boundary layer responses are observed, dominated by different processes. The inner portion of the boundary layer ($y/\delta < 0.4$) is dominated by the principal strain rate, whereas the outer portion ($y/\delta > 0.4$) is dominated by dilatation. This delineation in the dominant mechanisms significantly contributes to the restructuring of the turbulence within the boundary layer. Specifically, the Reynolds shear stress is positive within the principal strain-rate-dominated lower region, whereas it is near zero in the in the dilatation-dominated outer region (see figure 5*c*). Capturing this non-equilibrium behaviour represents a challenge from a modelling perspective.

4.2. *Reynolds stress modelling*

The above discussion motivates a study on whether or not Reynolds stress transport modelling can capture the redistributed stresses for this class of flow. Most algebraic and two-equation models use the Boussinesq approximation to compute the Reynolds stresses (see, e.g., Wilcox 2000). For this relation to hold for the present SPG case, the eddy viscosity μ_T would have be negative for $y/\delta > 0.4$. Current models do not routinely allow for negative eddy viscosities and the corresponding physical interpretation is unclear. Thus, it is expected that a Reynolds stress transport equation based closure is required to describe the turbulence response to the present pressure gradient driven strain-rate field.

To test this hypothesis, a simplified integration of the Reynolds shear stress transport equation was performed. The Launder, Reece & Rodi (1975) Reynolds stress transport model was selected, as it has been shown to be representative for this class of flow (Dussauge & Gaviglio 1987). It is emphasized here that this analysis is not intended to validate or calibrate the Launder *et al.* (1975) model. Instead, the goal is to

	C_1	C_2	C_3	C_3-1	C_4	C_5	C_6	C_7	$-\tau_{xx}/\rho k$	$-\tau_{yy}/\rho k$
LRR	1.50	0.40	0.76	−0.24	0.22	0.53	0.13	0.02	0.93	0.46
ZPG	1.03	0.56	0.78	−0.22	0.78	0.78	0.13	0.02	1.10	0.24
SPG	1.44	0.56	0.78	−0.22	0.22	0.53	0.13	0.02[a]	0.98	0.36

TABLE 5. Model constant summary. [a] This constant was adjusted to 0.06 for improved agreement for the SPG case.

qualitatively assess the applicability of this class of model to capture the Reynolds shear stress trends. Hence, a series of simplifications, relevant to the present flows, were performed to facilitate integration of the Launder *et al.* (1975) model.

First, the SPG strain-rate data in figure 4 demonstrated that the axial gradients were negligible compared with transverse gradients. Thus, neglecting the axial strain rates, diffusion and Reynolds stress gradients yields the following reduced formulation for the Launder *et al.* (1975) model:

$$\frac{\partial \tau_{xy}}{\partial t}+\tau_{xy}\frac{\partial V}{\partial y}\approx -C_1\frac{\varepsilon}{k}\tau_{xy}+(C_3-1)\left(\tau_{xy}\frac{\partial V}{\partial y}+\tau_{yy}\frac{\partial U}{\partial y}\right)+C_4\left(\tau_{xy}\frac{\partial V}{\partial y}+\tau_{xx}\frac{\partial U}{\partial y}\right)+\frac{1}{2}C_5\rho k\frac{\partial U}{\partial y}-\left[C_6\frac{\varepsilon}{k}\tau_{xy}-C_7\left(\tau_{yy}-\tau_{xx}\right)\frac{\partial U}{\partial y}\right]\frac{k^{3/2}}{\varepsilon y}. \tag{4.1}$$

On the left-hand side are the local time derivative and the convective term, resulting from dilatation. The first term on the right-hand side represents the slow-pressure strain term. Terms 2–4 are a combination of the production and the rapid pressure strain redistribution. The last term is a near-wall correction to the pressure redistribution. Launder *et al.* (1975) demonstrated that the model constants C_1 and C_2 are free parameters and that $C_3=(8+C_2)/11$, $C_4=(8C_2-2)/11$ and $C_5=(60C_2-4)/55$. Launder *et al.* (1975) set C_1 and C_2 to reproduce equilibrium homogeneous shear layer normal stresses, which are given by

$$-\tau_{xx}/\rho k-2/3=(8+12C_2)/33C_1 \tag{4.2a}$$

$$-\tau_{yy}/\rho k-2/3=(2-30C_2)/33C_1. \tag{4.2b}$$

The constants C_6 and C_7 were set to reconcile the model with increased anisoptropy (τ_{yy}/τ_{xx}) and reduced values of $-\tau_{xy}/\rho k$ associated with near-wall boundary effects, as compared with homogeneous shear flow. The Launder *et al.* (1975) constants are summarized in the first row of table 5.

Second, the terms in (4.1) were re-organized into the following form

$$\mathrm{d}\tau_{xy}/\mathrm{d}t+a_1^{xy}\tau_{xy}=a_2^{xy}, \tag{4.3}$$

where the coefficients are given by

$$a_1^{xy}(y)=(2-C_3-C_4)\frac{\mathrm{d}V}{\mathrm{d}y}+\left(C_1+C_6\frac{k^{3/2}}{\varepsilon y}\right)\frac{\varepsilon}{k} \tag{4.4a}$$

$$a_2^{xy}(y)=\left[(C_3-1)\tau_{yy}+C_4\tau_{xx}\tfrac{1}{2}C_5\rho k-C_7\left(\tau_{xx}-\tau_{yy}\right)\frac{k^{3/2}}{\varepsilon y}\right]\left(\frac{\mathrm{d}U}{\mathrm{d}y}\right). \tag{4.4b}$$

Reduction of (4.1) to the ordinary differential form in (4.3) resulted from assuming that the coefficients in (4.4) are time invariant, and the numerical values were

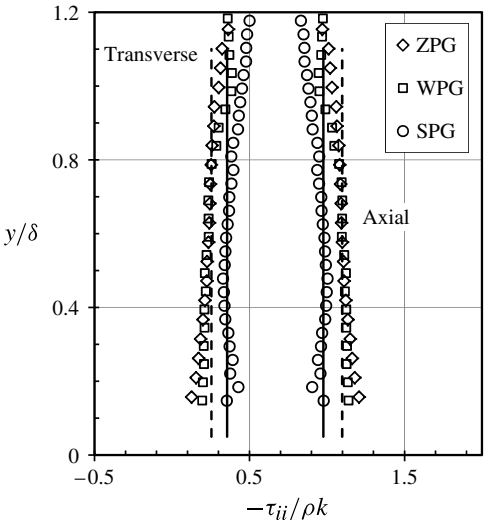

FIGURE 13. Model constant calibration. Open symbols show the data, whereas the lines show the fits to the data from which the model constants are extracted.

evaluated with the upstream ZPG Reynolds stresses from the data shown in figure 5, as well as the corresponding ZPG, WPG and SPG strain rates, as shown in figure 4. To evaluate the wall-correction terms, the turbulence time and length scales were estimated using the Boussinesq approximation for a standard $k-\varepsilon$ model (see Wilcox 2000). Specifically, for the ZPG flow, $\varepsilon/k \sim C_\mu/a_1 \partial U/\partial y$ (Bowersox 2009), where $C_\mu = 0.09$ and the Townsend (1961) constant, a_1, was set to 0.3, following Bradshaw, Ferris & Atwell (1967).

Third, (4.3) was integrated via an integrating factor to give

$$\tau_{xy}(y,t) \approx \frac{a_2^{xy}}{a_1^{xy}}(1 - e^{-a_1^{xy} t^*}) + \tau_{xy}^{ZPG}(y) e^{-a_1^{xy} t^*}. \tag{4.5}$$

With the normalizations in figures 4 and 5, the integration time, t^*, is given by tU_e/δ and was set to 6.2, corresponding to a convection length ($L = t^*\delta$) of 5.3 cm, which is the distance between where the curvature started and the measurement location. Once (4.5) was evaluated with the ZPG turbulence data, the resulting Reynolds stresses were transformed to the WPG and SPG coordinate systems using the rotations listed in table 3. Thus, (4.5), although severely reduced, represents a convenient theoretical test bed for model assessment.

For the present study, C_1 and C_2 were determined by evaluating the normal stresses on the left-hand sides of (4.2) with the average measured values for $y/\delta = 0.4$–0.8 (see figure 13). To estimate the turbulent kinetic energy, the spanwise normal stress was assumed to be the average of the axial and transverse components, which is consistent with reported trends (see e.g. Wilcox 2000). Thus, $\rho k = -3(\tau_{xx} + \tau_{yy})/4$. The resulting model constants for the ZPG and SPG cases are listed in the second and third rows of table 5. The WPG values were essentially the same as those for the ZPG flow (see figure 14). The last two columns summarize the axial and transverse normal stresses. The ZPG model constants correspond to $-\tau_{xx}/\rho k = 1.1$ and $-\tau_{yy}/\rho k = 0.24$, where for the original Launder *et al.* (1975) constants, $-\tau_{xx}/\rho k = 0.93$ and $-\tau_{yy}/\rho k = 0.46$. These differences reflect the increased anisotropy shown

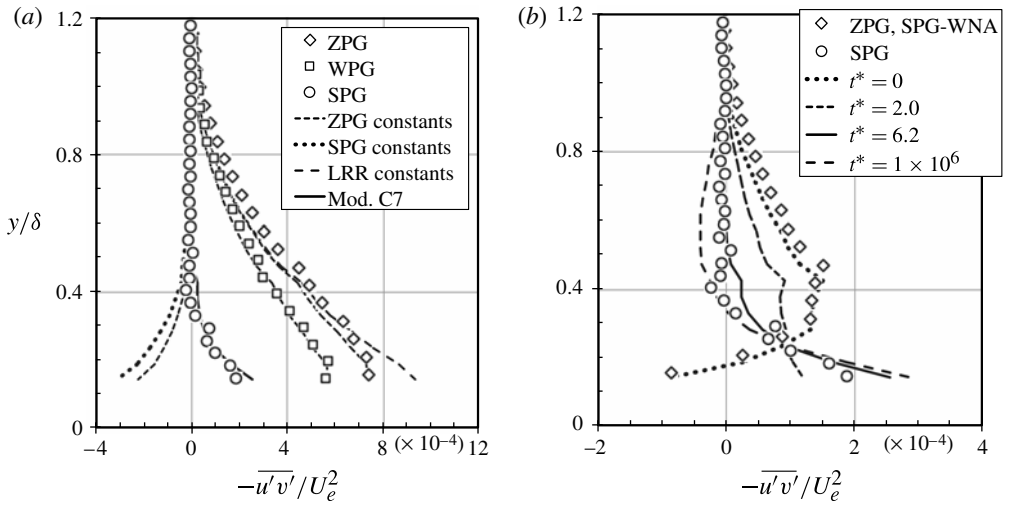

FIGURE 14. Reynolds shear stress model predictions using (4.3): (*a*) Reynolds shear stress predictions ($t^* = 6.2$); (*b*) predicted SPG evolutions on an exploded scale. ZPG, SPG-WNA: ZPG data transformed to the SPG wall normal axes. See the text for definitions of model constants.

in figure 2(*b*) for the supersonic studies as compared to their low-speed counterpart. Additional compressibility and/or Reynolds number corrections were not included, as those effects were inherently accounted for when setting the constants to match the present normal stresses. For the SPG flow, the axial and transverse stresses were both reduced (see figure 5). The corresponding values of C_1 and C_2, computed from these stresses, following procedure used for the ZPG case, are listed in table 5.

Comparisons, with constants set to the values listed in table 5, are shown in figure 14(*a*). The model predictions with the ZPG constants are given by the short dashed lines. The model predictions and experimental data are in good quantitative agreement, to within the expected measurement uncertainties, across the boundary layer. The original Launder *et al.* (1975) constants also produced reasonable agreement for the ZPG case (long dashes) except near the wall, where the shear stresses are over-predicted. For the SPG case, the model was evaluated with both the SPG (solid line) and ZPG constants (short dashes). The model, with both sets of constants, predicted the large SPG reduction in the Reynolds shear stress. The agreement with the data in the outer 50–60 % of the boundary layer appears to have been qualitatively correct. However, the reduction was over predicted in the lower 40 %. Because the departures were near the wall, an *ad hoc* adjustment of the near-wall correction was investigated. This seems to be a reasonable line of inquiry, given that the present simplified form of the model did not attempt to capture the effects of the distortion on the time and length scales associated with the near-wall term. Reducing C_6 and/or increasing C_7 was found to provide a means to control model output. For simplicity, C_7 was increased to 0.06 to achieve the agreement shown in figure 14(*a*) (solid line). Although this correction is not rigourous, the results in figure 14(*a*) suggest that the Launder *et al.* (1975) stress transport model, with modest recalibration, naturally captures the Reynolds stresses shown in figure 5(*c*), including the SPG case. This assessment was the primary purpose of the analysis.

The predicted time evolution of the Reynolds stresses for the SPG case, with the modified SPG model constants, is shown in figure 14(*b*). The results are plotted on an exploded scale in the SPG wall normal coordinate system for clarity. As indicated, the initial condition for the calculations was the predicted ZPG flow, which compares favourably with the ZPG measurements (open diamonds on figure 14(*b*)). As the integration time is increased, the model results monotonically decrease. The prediction reaches an asymptotic value for $t^* > 20$. The $t^* = 1 \times 10^6$ line shows this asymptote. This asymptote is important, as it indicates a limiting value for the Reynolds shear stress reduction for the present distortion. The present data lying close to this limit suggests that the turbulence responds rapidly to the distortion.

The limiting behaviour for large t^* also provides insight into the modelled flow dynamics. In this limit, $\tau_{xy}(y, t) \approx a_2^{xy}/a_1^{xy}$. Focusing first on a_1^{xy} in the denominator, it is apparent that given the constants listed in table 5, the coefficient premultiplying $\mathrm{d}V/\mathrm{d}y$ is $O(1)$ (see (4.4)). Thus, the overall magnitude of the additional strain-rate term is comparable with the second term in a_1^{xy} in (4.4), as C_1 is in the range of 1–1.5 and ε/k was modelled as $C_\mu/a_1 \partial U/\partial y$, where $C_\mu/a_1 \approx 0.3$. Hence, the favourable $\mathrm{d}V/\mathrm{d}y$ strain rates have a significant stabilizing (decreasing) effect on the Reynolds stress as compared to the ZPG flow, where $\mathrm{d}V/\mathrm{d}y = 0$. This effect was most pronounced in the outer region of the boundary layer, where $\mathrm{d}V/\mathrm{d}y > \mathrm{d}U/\mathrm{d}y$. This is consistent with the general conclusion from Dussauge & Gaviglio (1987) that dilatation is a driving stabilizing mechanism in favourable pressure gradient supersonic flows. Importantly, because it was shown earlier that $\mathrm{d}V/\mathrm{d}y$ is effectively constant throughout the boundary layer, it can be surmised that the decreasing main strain rate $\mathrm{d}U/\mathrm{d}y$ is primarily responsible for this effect.

The model also reveals that increasing the dissipation will have a stabilizing effect on the Reynolds shear stress. It is expected, although not shown, that the increased kinematic viscosity associated with the reduced temperature will result in increased dissipation in the favourable pressure gradient region of the flow. Focusing now on a_2^{xy}, it is apparent that the numerator in the above limiting Reynolds shear stress has the form of a production term associated with the principal strain rate, $\partial U/\partial y$. Thus, the predicted magnitude and sign of the Reynolds shear stress result from an intricate balance between the axial and transverse normal stresses associated with the production and the rapid pressure redistribution, where the coefficients listed in table 5 provide the relative weighting. This balance is the net result of the underlying turbulence structure.

5. Summary and conclusions

An experimental study has been carried out to investigate the influence of streamline curvature-driven pressure gradients on the turbulence structure of a Mach 4.9, high-Reynolds-number ($Re_\theta = 43\,000$) boundary layer. The steps in the study were to: (i) characterize the influence of the pressure gradients on the mean velocity and strain-rate field; (ii) quantify the role of the strain-rate field on the Reynolds stress turbulence statistics; and (iii) analyse the effect of the strain rates on the underlying turbulence structure.

The results suggest that the favourable pressure gradient had an overall stabilizing effect on the boundary layer, while preferentially affecting the turbulent flow structures based on their distance from the wall. More pronounced reorientation occurred in the outer part of the boundary layer, whereas a reduction in structure size was more pronounced nearer the wall. The principal strain rates responsible for the turbulence

modifications were dU/dy and dV/dy, although it was essentially the decrease in dU/dy that was responsible for the observed trends; dV/dy remained essentially constant throughout most of the boundary layer. The Reynolds-averaged normal and shear stresses followed the expected stabilizing trends, where the Reynolds shear stress for the strongest favourable pressure gradient considered was observed to be practically zero and perhaps slightly negative. These results indicate that there could be decaying turbulent motions within this region of the boundary layer and that the mean flow was possibly extracting energy from the turbulent flow structures. When viewed within the context of previous studies, this energy shift appeared to be a function of pressure gradient strength parameters, rather than the pressure gradient geometry.

Quadrant decomposition results demonstrated significant redistribution in the boundary layer turbulence, where the transverse and normal stresses became more balanced and the cross-correlation (i.e. Reynolds shear stress) decomposition was modified from the ZPG Q2–Q4 event-dominated ellipse, to become a significantly more balanced distribution. Little preferential quadrant mode selection was observed for the strongest pressure gradient case considered and the Reynolds stress components exhibited reduced contributions, which suggests reduced fluctuations. Consistent with earlier work, this stabilizing effect implies a weakening of the turbulent structure organization. The structural results, when taken with the overall turbulence levels, suggest that large-scale processes (i.e. convection, production and redistribution) control the basic changes. Large-eddy methods should therefore be able to adequately capture the streamline curvature driven pressure gradient effects described in this study.

Integration of a simplified form of the Launder *et al.* (1975) Reynolds stress transport closure model provided a framework to assess the role of the strain-rate field on the observed Reynolds shear stresses. The analysis helped to explain the observed sign change in the shear stress and demonstrated that Reynolds stress transport closure has the potential to adequately capture the salient features associated with this class of flow given proper knowledge of the evolution of the underlying model parameters, which are determined by the basic structure of the evolving turbulence itself.

Acknowledgements

The authors gratefully acknowledge Dr J. Schmisseur of the Air Force Office of Scientific Research (AFOSR) for sponsoring this work through GRANT FA9550-08-1-0093. The authors also acknowledge the AFOSR/NASA National Center for Hypersonic Research in Laminar–Turbulent Transition through Grant FA9550-09-1-0341. Lastly, the authors thank Scott Peltier for his assistance in the experimental campaign.

REFERENCES

ADRIAN, R., MEINHART, C. & TOMKINS, C. 2000 Vortex organization in the outer region of the turbulent boundary layer. *J. Fluid Mech.* **422**, 1–54.

ARNETTE, S., SAMIMY, M. & ELLIOTT, G. 1995 Structure of supersonic turbulent boundary layer after expansion regions. *AIAA J.* **33** (3), 430–438.

ARNETTE, S., SAMIMY, M. & ELLIOTT, G. 1998 The effects of expansion on the turbulence structure of compressible boundary layers. *J. Fluid Mech.* **367**, 67–105.

BENEDICT, L. & GOULD, R. 1996 Towards better uncertainty estimates for turbulence statistics. *Exp. Fluids* **22**, 129–136.

BRADSHAW, P. 1969 The analogy between streamline curvature and buoyancy in turbulent shear flow. *J. Fluid Mech.* **36**, 177–191.

BRADSHAW, P. 1973 The effect of streamline curvature on turbulent flow. *AGARDograph* **169**.

BRADSHAW, P. 1974 The effect of mean compression or dilatation on the turbulence structure of supersonic boundary layers. *J. Fluid Mech.* **63** (3), 449–464.

BRADSHAW, P. 1977 Compressible turbulent shear layers. *Annu. Rev. Fluid Mech.* **9**, 33–54.

BRADSHAW, P., FERRIS, D. & ATWELL, N. 1967 Calculation of boundary layer development using the turbulent energy equation. *J. Fluid Mech.* **28**, 593–616.

BOWERSOX, R. 2009 Extension of equilibrium turbulent heat flux models to high-speed shear flows. *J. Fluid Mech.* **633**, 61–70.

CLAUSER, F. H. 1956 The turbulent boundary layer. In *Advanced Applied Mechanics*, vol. 4, pp. 1–51. Academic.

COLES, D. 1956 The law of the wake in the turbulent boundary layer. *J. Fluid Mech.* **1**, 191–226.

DONOVAN, J., SPINA, E. & SMITS, A. 1994 The structure of a supersonic turbulent boundary layers subjected to concave surface curvature. *J. Fluid Mech.* **259**, 1–24.

DUAN, L. & MARTIN, M. P. 2011 Direct numerical simulation of hypersonic turbulent boundary layers. Part IV: effect of high enthalpy. *J. Fluid Mech.* **684**, 25–59.

DUSSAUGE, J. P. & GAVIGLIO, J. 1987 The rapid expansion of a supersonic turbulent flow: role of bulk dilatation. *J. Fluid Mech.* **174**, 81–112.

ECKER, T., LOWE, K. & SIMPSON, R. Novel laser Doppler acceleration measurements of particle lag through a shock wave, *AIAA Paper* 2012-0694, 2012.

EKOTO, I., BOWERSOX, R., BEUTNER, T. & GOSS, L. 2009 Response of supersonic turbulent boundary layers to local and global mechanical distortions. *J. Fluid Mech.* **630**, 225–265.

ELENA, M., LACHARME, J. P. & GAVIGLIO, J. 1985 Comparison of hot-wire and laser Doppler anemometry methods in supersonic turbulent boundary layers. In *Proc. Intl Symp. on Laser Anemometry*, pp. 151–157 ASME.

GANAPATHISUBRAMANI, B. 2007 Statistical properties of streamwise velocity in a supersonic turbulent boundary layer. *Phys. Fluids* **19**.

GANAPATHISUBRAMANI, B. 2008 Statistical structure of momentum sources and sinks in the outer region of a turbulent boundary layer. *J. Fluid Mech.* **606**, 225–237.

GANAPATHISUBRAMANI, B., HUTCHINS, N., HAMBLETON, W. T., LONGMIRE, E. K. & MARUSIC, I. 2005 Investigation of large-scale coherence in a turbulent boundary layer using two-point correlations. *J. Fluid Mech.* **524**, 57–80.

HERRIN, J. & DUTTON, J. 1997 The turbulence structure of a reattaching axisymmetric compressible free shear layer. *Phys. Fluids* **9**, 3502–3512.

HINZE, J. 1975 *Turbulence*. McGraw-Hill.

HOPKINS, E. 1972 Charts for predicting turbulent skin friction from the van Driest Method (II), NASA TN – D-6945, Washington DC.

HUMBLE, R. A., PELTIER, S. J. & BOWERSOX, R. D. W. 2012 Visualization of the structural response of a hypersonic turbulent boundary layer to convex curvature. *Phys. Fluids* **24** (10), 24–48.

Innovative Scientific Solutions, Inc. 2005. dPIV, 32-bit PIV Analysis Code, Software Package, Version 2.1, Innovative Scientific Solutions, Inc., Dayton, OH.

KLEBANOFF, P. S. 1955 Characteristics of Turbulence in a Boundary Layer with Zero Pressure Gradient, NACA Rep. 1247.

KLINE, S., REYNOLDS, W., SCHRAUB, F. & RUNSTADLER, P. 1967 The structure of turbulent boundary layers. *J. Fluid Mech.* **30**, 741–773.

KROGSTAD, P.-A. & SKARE, P. E. 1995 Influence of a strong adverse pressure gradient on the turbulent structure in a boundary layer. *Phys. Fluids* **7**, 2014–2024.

LAUNDER, B., REECE, G. & RODI, W. 1975 Progress in the development of a Reynolds-stress turbulence closure. *J. Fluid Mech.* **68** (3), 537–566.

LEWIS, J., GRAN, R. & KUBOTA, T. 1973 An experiment on the adiabatic compressible turbulent boundary layer in adverse and favourable pressure gradients. *J. Fluid Mech.* **51**, 657–672.

LU, S. S. & WILLMARTH, W. W. 1973 Measurements of the structure of the Reynolds stress in a turbulent boundary layer. *J. Fluid Mech.* **60**, 481–511.

LUKER, J., BOWERSOX, R. & BUTER, T. 2000 Influence of curvature-driven favourable pressure gradient on supersonic turbulent boundary layer. *AIAA J.* **38** (8), 1351–1359.

MCDONALD, H. 1968 The departure from equilibrium of turbulent boundary layers. *Aeronaut. Q.* **XIX Pt. 1**, 1–19.

MEI, R. 1996 Velocity fidelity of flow tracer particles. *Exp. Fluids* **22**, 1–13.

MORKOVIN, M. 1961 Effects of compressibility on turbulent flows. In *The Mechanics of Turbulence*, pp. 367–380. Gordon and Breach Science.

NAGIB, N. M & CHAUHAN, K. A. 2008 Variations of von Karman coefficient in canonical flows. *Phys. Fluids* **20**, 101518.

NOLAN, K. P., WALSH, E. J. & MCELIGOT, D. M. 2010 Quadrant analysis of a transitional boundary layer subject to free stream turbulence. *J. Fluid Mech.* **658**, 310–335.

PANIGRAHI, P. K., SCHROEDER, A. & KOMPENHANS, J. 2008 Turbulent structures and budgets behind permeable ribs. *Exp. Therm. Fluid Sci.* **32**, 1011–1033.

POPE, S. 2000 *Turbulent Flows*. Cambridge University Press.

RAFFEL, M., WILLERT, C., WERELEY, S. & KOMPENHANS, J. 2007 *Particle Image Velocimetry*. Springer.

RAUPACH, M. 1981 Conditional statistics of Reynolds stress in rough-wall and smooth-wall turbulent boundary layers. *J. Fluid Mech.* **108**, 363–382.

RINGUETTE, M., BOOKEY, P., WYCKHAM, C. & SMITS, A. 2009 Experimental study of a Mach 3 compression ramp interaction at $Re_\theta = 2400$. *AIAA J.* **47** (2).

RINGUETTE, M., WU, M. & MARTIN, P. 2008 Coherent structures in direct numerical simulation of turbulent boundary layers at Mach 3. *J. Fluid Mech.* **594**, 59–69.

SCHETZ, J. 1993 *Boundary Layer Theory*. Prentice Hall.

SCHULTZ-GRUNOW, F. 1940 A new resistance law for smooth plates. *Luftfahrtforschung* **17**, 239–246.

SMITS, A. J. & DUSSAUGE, J.-P. 2006 Turbulent Shear Layers in Supersonic Flow.

SPALDING, D. B. 1961 A single formula for the law of the wall. *J. Appl. Mech.* **28**, 455–457.

SPINA, E. F., SMITS, A. J. & ROBINSON, S. 1994 The physics of supersonic turbulent boundary layers. *Annu. Rev. Fluid Mech.* **26**, 287–319.

SMITS, A. J., SPINA, E. F., ALVING, A. E., SMITH, R. W., FERNANDO, E. M. & DONOVAN, J. F. 1989 A comparison of the turbulence structure of subsonic and supersonic boundary layers. *Phys. Fluids* A **1** (11), 1865–1875.

TOWNSEND, A. 1961 Equilibrium layers and wall turbulence. *J. Fluid Mech.* **11**, 97–120.

TSI, Inc. 2003. Model 9306A Six-Jet Atomizer Instruction Manual, 1930099, Revision B. TSI, Inc., Shoreview, MN.

VAN DRIEST, E. R. 1956 The problem with aerodynamic heating. *Aeronaut. Engng Rev.* **15**, 26–41.

WHITE, F. 2006 *Viscous Fluid Flow*, 3rd edn. McGraw-Hill.

WILCOX, D. 2000 *Turbulence Modeling for CFD*. DCW Industries.

ZAGAROLA, M. V. & SMITS, A. J. 1998 Mean-flow scaling of turbulent pipe flow. *J. Fluid Mech.* **373**, 33–79.